Volume 26
Number 38
14 October 2024
Pages 5301–5480

CrystEngComm

rsc.li/crystengcomm

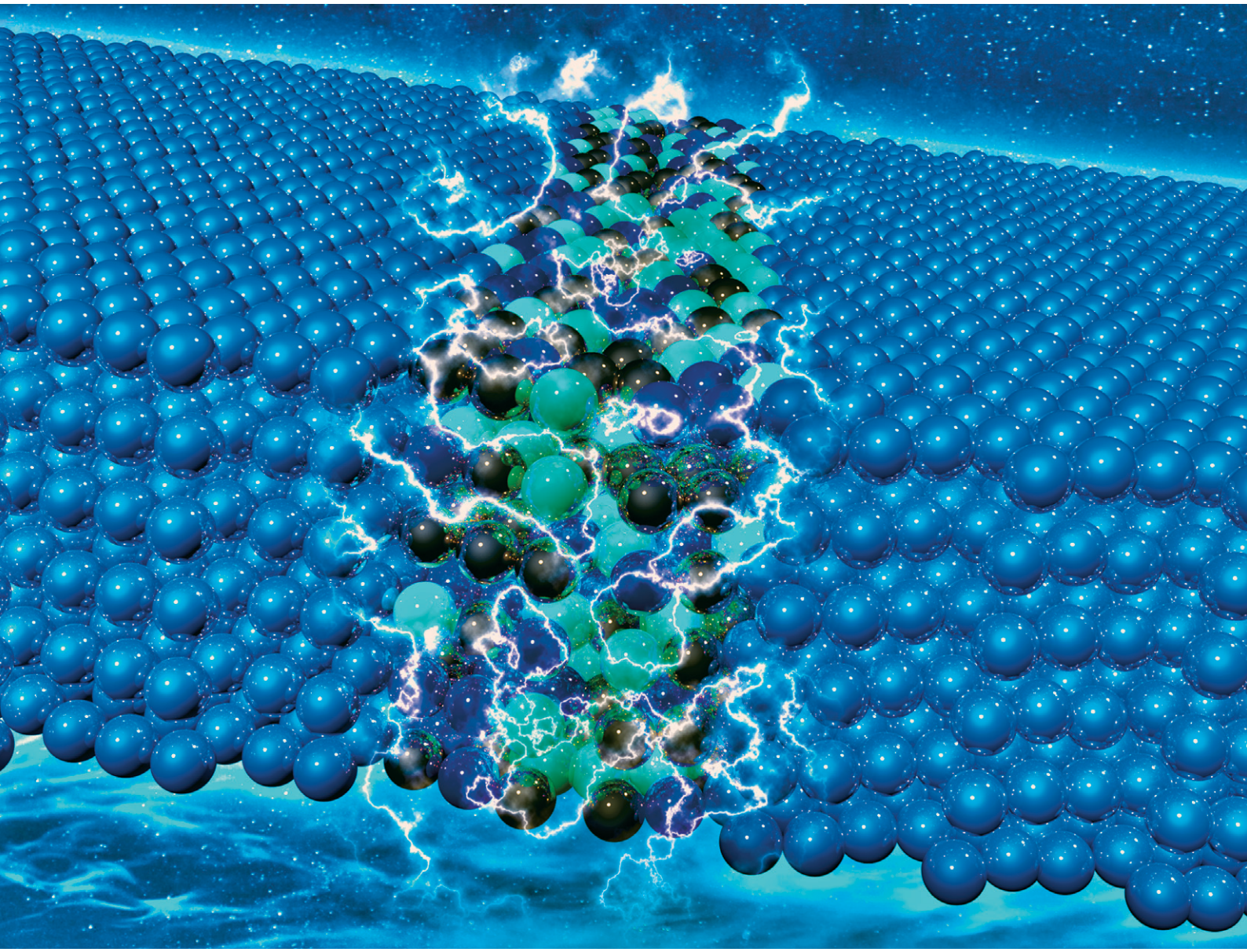

ISSN 1466-8033

ROYAL SOCIETY OF CHEMISTRY

PAPER

Tao Fu, Shayuan Weng *et al.*
Effect of grain boundary doping/segregation on the mechanical behavior of Ta bicrystal

CrystEngComm

ROYAL SOCIETY OF CHEMISTRY

PAPER

View Article Online
View Journal | View Issue

Cite this: *CrystEngComm*, 2024, **26**, 5324

Effect of grain boundary doping/segregation on the mechanical behavior of Ta bicrystal†

Yang Pan,[a] Tao Fu, *[a] Hao Hu,[a] Xingjie Chen,[b] Chuanying Li[a] and Shayuan Weng*[ac]

The introduction of foreign atoms significantly alters the grain boundary (GB) behavior in materials, consequently affecting their mechanical properties. However, the effects of random doping and GB segregation of foreign atoms on deformation mechanisms and mechanical properties remain unknown. In this work, the GB behavior and deformation mechanisms of Ta bicrystals under various element doping and segregation conditions were investigated using molecular dynamics simulation. The results reveal that the deformation mechanism of pure Ta bicrystals involves dislocation slip and twinning initiated from GBs. Notably, both GB doping and segregation induce BCC to FCC phase transformations, which is attributed to the non-uniform displacement of atoms in the {112} plane along the ⟨111⟩ direction. Doping with W and Mo elevates the yield stress, whereas doping with Nb exhibits an inverse effect. Remarkably, the segregation of W, Mo, and Nb significantly enhances mechanical properties, surpassing the effects of GB doping. This segregation modifies the GB composition, reduces GB energy, and enhances GB stability. Our study sheds light on the pivotal role of GB doping and segregation in improving the mechanical properties and understanding the deformation mechanisms of nanocrystalline materials, offering vital insights for future material design and engineering.

Received 17th June 2024,
Accepted 6th September 2024

DOI: 10.1039/d4ce00603h

rsc.li/crystengcomm

1. Introduction

Grain boundaries (GBs) are common planar defects that play a crucial role in determining the properties of polycrystalline materials.[1–4] In contrast to the stable grain interior, GBs possess higher energy and excess free volume, making them less stable and mechanically weaker.[5] The movement of dislocations along GBs can lead to local stress concentration, which may result in the formation of cracks or voids from GBs, potentially leading to intergranular fracture.[6–8] On the other hand, the interaction between GBs and dislocations, particularly the resistance offered by GBs to dislocation movement, contributes to improving the mechanical properties of materials. As the grain size decreases, the proportion of GBs increases, thereby intensifying the hindrance to dislocation motion and markedly enhancing the mechanical properties (known as the Hall–Petch relation).[9] However, conventional plastic deformation reduces grain sizes to the submicrometer range, mainly forming high-angle GBs that exhibit higher energy and excess free volume, along with lower thermal and mechanical stability compared to low-angle GBs.[10] The thermal instability of refined grains increases their tendency for grain coarsening in contrast to larger grains.[11] In fact, in the case of nanograined pure copper, grain coarsening can occur even at room temperature.[12] The limited mechanical and thermal stabilities of nanograined metals pose significant challenges for their processing and technological applications. Hence, there is a growing interest in enhancing GB performance to mitigate the limitations of nanocrystalline materials.

Raabe *et al.* introduced the concept of "grain boundary segregation engineering" to manipulate the compositions, structures, and properties of GBs through solute decoration.[13] This approach enables the customization of specific GB behaviors to achieve desired mechanical properties.[10,14] For instance, the segregation of Mo atoms has been demonstrated to reduce the energy and mobility of GB in nanocrystalline Ni.[15] In a study by Fan *et al.*, the segregation of Nb atoms into GBs effectively inhibited GB precipitation and migration in CoCrFeNi-based high entropy alloys, attributed to the synergistic effect of decreased GB energy and solute drag.[16] Moreover, both experimental and theoretical investigations have demonstrated that solute segregations can enhance GB stability and intergranular cohesion in metals, such as Al,[17,18] Cu,[19,20] Fe,[21–23] and others.

[a] *Department of Engineering Mechanics, Chongqing University, Chongqing 400044, China. E-mail: futao@cqu.edu.cn*
[b] *School of Aerospace, Xi'an Jiaotong University, Xi'an 710049, China*
[c] *College of Mechanical and Electrical Engineering, Hohai University, Changzhou 213022, China. E-mail: syweng@hhu.edu.cn*

† Electronic supplementary information (ESI) available. See DOI: https://doi.org/10.1039/d4ce00603h

The segregation of elements at GBs alters their structure and properties, thereby affecting the dominant deformation mechanisms. In a study by Ma *et al.*, the plastic deformation of an Al $\Sigma9(221)[1\bar{1}0]$ bicrystal under tension was characterized by the nucleation of Shockley partial dislocations and intrinsic stacking faults (ISFs) from the GBs, which then propagated along the {111} plane into the grains. The observed segregation of Mg atoms enhanced the stability of the GB structure and raised the critical stress for dislocation nucleation, thereby impeding the propagation of ISFs.[24] Similarly, Pal *et al.* identified a pinning effect induced by Zr segregation, which enhanced the stability of GBs and restrained their distortion and migration during shear, thereby shifting the deformation mode towards dislocation nucleation and motion from the free surface. Under bending creep loading, the reduced mobility of GB due to Zr segregation prompted a transition from GB migration-mediated deformation to dislocation and twin-mediated deformation.[25] Yang *et al.* reported that the deformation mechanism of W $\Sigma3(111)$ bicrystals under tension was primarily governed by dislocations and stacking faults, with Cu segregation into GBs suppressing the formation and growth of these defects, thereby reducing their hindrance to crack propagation.[26] While current research largely focuses on elucidating the impact of GB segregation on mechanical behaviors,[27–32] further studies are needed to explore the effects of random element doping near GBs (*i.e.*, element doping) on deformation mechanisms and mechanical properties of materials. Additionally, a comparative analysis of element doping and segregation, including similarities and differences, remains an important area for future investigation.

GBs are commonly categorized into high-angle and low-angle GBs based on the misorientation between adjacent grains. High-angle GBs generally possess higher energy and lower stability,[10] significantly affecting GB-mediated deformation kinetics and materials strength. Molecular dynamics (MD) simulation is an effective method for exploring the relationship between material microstructures and mechanical properties,[33,34] offering atomic-level insights into plastic deformation,[35] microstructural evolution,[36] and GB behavior.[37–39]

In this work, we focused on the Ta $\Sigma3(11\bar{1})\langle110\rangle$ high-energy symmetric tilt GB[40] and employed MD simulation to investigate the mechanical response and deformation mechanisms of Ta bicrystals under various doping and segregation conditions. This article is organized as follows: section 2 outlines the simulation methodology; section 3 presents the deformation mechanisms and mechanical responses of Ta bicrystals under shear loading with various element doping/segregation; section 4 discusses the deformation mechanisms, comparing the effects of element doping and segregation on mechanical properties; and section 5 provides a conclusion summarizing our work.

2. Method

To establish a stable GB structure, Ta bicrystal samples are constructed following the method described by Tschopp *et al.*[41] Fig. 1(a) illustrates a schematic diagram of the Ta bicrystal sample, consisting of two symmetric grains (upper and lower) separated by a GB. Periodic boundary conditions are applied in the x and z directions, while free boundary conditions are used in the y direction. The sample dimensions are 227 Å × 182 Å × 33 Å, containing a total of 74 480 atoms. The green region, spanning 40 Å above and below the GB in Fig. 1(a), is designated as the doping/segregation (D/S) region. Transition metals, W, Mo, and Nb, are selected as foreign atoms due to their similar atomic sizes to that of Ta, which helps maintain lattice integrity during doping, reduces lattice distortion, and promotes a uniform distribution of doping elements at the Ta GBs. In the doped samples, a specified percentage of Ta atoms in the D/S region are randomly selected and replaced with W/Mo/Nb (referred to as GB doping). For the segregated samples, additional Monte Carlo (MC) simulations[42,43] are performed to obtain the stable configuration considering atomic segregation (referred to as GB segregation). Fig. 1(b) and (c) show the element distribution in the D/S region of the Nb-doped and Nb-segregated Ta bicrystal samples at a concentration of 5%, respectively. In the doped sample, Nb atoms are randomly distributed [Fig. 1(b)], whereas in the segregated sample, Nb atoms tend to segregate towards the GB [Fig. 1(c)]. Thus, the key distinction is that doped samples display a random distribution of foreign atoms, while segregated samples show a directional aggregation. We employ a machine learning potential developed by Li *et al.*[44] to describe the interactions among Nb, Mo, Ta, and W atoms. This potential has been validated for its efficacy in describing the fundamental physical and mechanical properties of this system, including elastic constants, generalized stacking fault energy (GSFE), and dislocation core structures.[44] It has also been applied to study the plastic[33] and GB behavior[45] of this system.

Before loading, the sample undergoes energy minimization using the conjugate gradient algorithm to optimize the GB structure. To mitigate the potential interference of thermal effects on mechanical responses and deformation mechanisms, the mechanical test simulations are conducted at a temperature of 0.1 K. The sample is then fully relaxed at this temperature under NPT ensemble to achieve a stable state. The regions at the top and bottom of the sample with a thickness of approximately 11 Å are designated as clamps (rigid plates) to execute deformation. The atoms in these regions are frozen, as shown in Fig. 1(a). During loading, the top rigid plate is displaced along the positive X-axis, while the bottom rigid plate remains fixed, inducing shear deformation of the sample at a strain rate of 1×10^8 s^{-1}. All simulations are conducted using the open-source code LAMMPS,[46] with visualization carried out using OVITO.[47] The dislocation extraction algorithm (DXA)[48] and

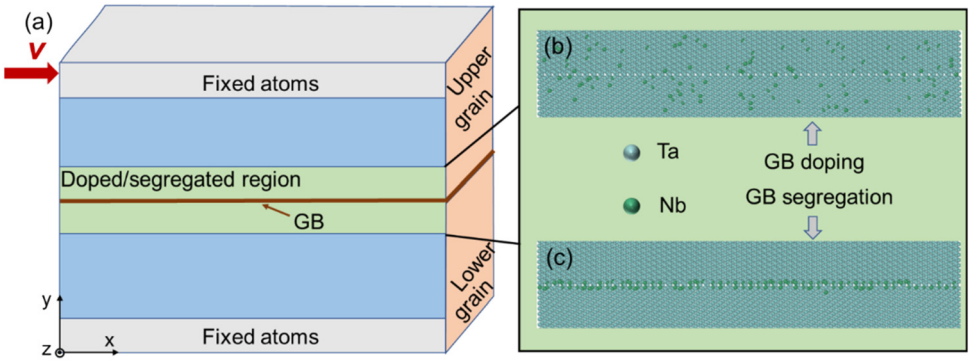

Fig. 1 MD simulation of shear of Ta bicrystal with GB doping/segregation. (a) Schematic diagram of Ta bicrystal sample. (b) and (c) Atomic distribution within the doping/segregation (D/S) region of doped and segregated samples.

common neighbor analysis (CNA),[49,50] implemented in OVITO are utilized to identify dislocations and GBs.

3. Results

3.1 GB behavior of pure Ta bicrystal under shear

Fig. 2(a) presents the shear stress–strain (τ–γ) curve of the pure Ta bicrystal sample, with characteristic points labeled as A–D. The corresponding microstructures are displayed in Fig. 2(b) and (c). Initially, the sample experiences elastic deformation, characterized by a linear stress–strain relationship [Fig. 2(a)]. Upon reaching the yield point, a sudden drop in stress signifies the onset of plastic deformation. Prior to significant plastic deformation, GBs undergo coarsening, as evidenced in Fig. 2(b) A and B, due to the activation of the $\{112\}\langle 111\rangle$ slip system at the GBs. The slight incomplete slip leads to the observable "GB coarsening". As γ increases, twins and $a/2\langle 111\rangle$ edge dislocations nucleate from the GB, as illustrated in Fig. 2(b) C and (c) C, respectively. The subsequent continuous nucleation and motion of dislocations and twins release the elastic strain energy stored [Fig. 2(c)], resulting in a sudden stress drop [points C to D in Fig. 2(a)]. In our bicrystal samples, the grain interiors are defect-free, leading to stress

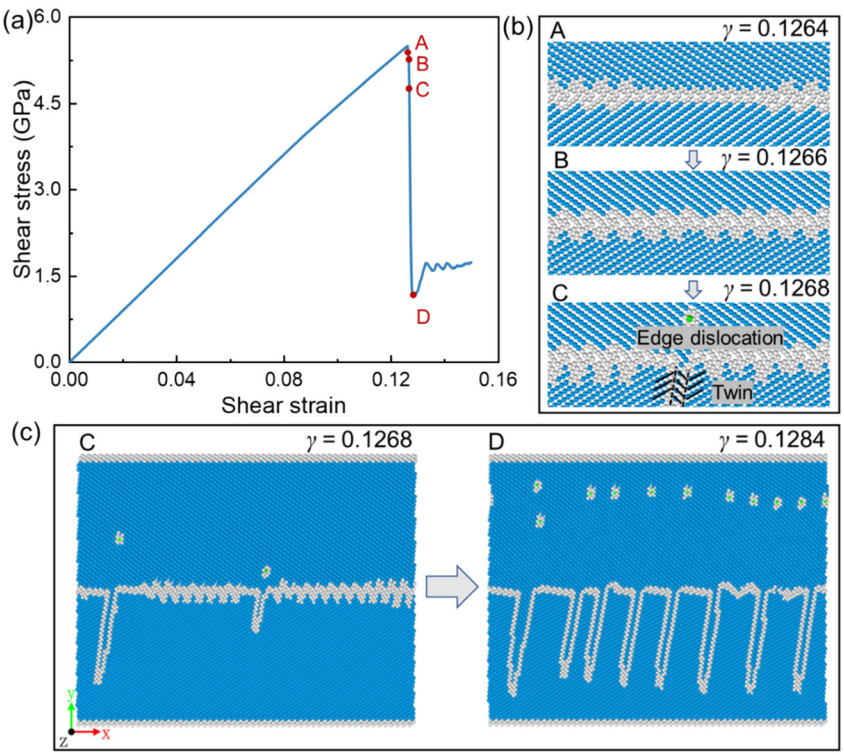

Fig. 2 GB behavior and mechanical response of pure Ta bicrystal with $\Sigma 3(11\bar{1})\langle 110\rangle$ GB under shear. (a) Shear stress–strain (τ–γ) curve of pure Ta bicrystal under shear, with characteristic points labeled as A–D. (b) Microstructure snapshots at points A to C in Fig. 2(a), depict "GB coarsening" and subsequent nucleation of twins and $a/2\langle 111\rangle$ edge dislocations. (c) Microstructure snapshots at points C and D in Fig. 2(a), show the continuous nucleation and movement of twins and dislocations leading to stress drop.

concentration primarily at GBs. During loading, defects such as dislocations begin to nucleate from the GBs, causing a rapid release of accumulated elastic strain energy. This leads to a sharp drop in stress, distinct from typical plastic deformation. This phenomenon has been widely observed in studies of bicrystals under shear.[25,45,51] In conventional plastic behavior, defects such as dislocation and stacking faults are typically pre-existing in the crystal. These defects are activated when the applied stress reaches a specific threshold. The energy released during the nucleation and glide of a new dislocation is usually significantly larger than that required for the motion of existing ones, leading to a considerable stress drop rather than a gradual evolution of typical plasticity.

To analyze the twinning process, Fig. 3(a) provides a magnified view of the atomic distribution on the {110} plane of the lower grain. During shear, the formation of four-layer isosceles twins is observed, which differs from the traditional three-layer reflection twins.[52] This process involves the decomposition of the $a/6[\bar{1}\bar{1}1]$ partial dislocation into two $a/12[\bar{1}\bar{1}\bar{1}]$ dislocations, which then glide simultaneously on adjacent $(11\bar{2})$ planes along the $[\bar{1}\bar{1}\bar{1}]$ direction. The sequential movement of these $a/12[\bar{1}\bar{1}\bar{1}]$ dislocations on the $(11\bar{2})$ planes layer by layer leads to the formation of twins, as schematically illustrated in Fig. 3(b). To elucidate the formation of isosceles twins during shear rather than reflection twins, we calculate the GSFE for both types of twins [Fig. 3(c)], where γ_{iso}^{usf} and γ_{ref}^{usf} represent energy barriers associated with the nucleation of the isosceles twin and reflection twin, respectively. Notably, γ_{iso}^{usf} is lower γ_{ref}^{usf}, making the isosceles twins energetically more favorable and easier to nucleate than the reflection twins.

3.2 Effects of GB doping

3.2.1 Mechanical response of sample with GB doping. Fig. 4(a)–(c) show the shear stress–strain curves of Ta bicrystal with $\Sigma3(11\bar{1})\langle110\rangle$ GB doped with various concentrations (c = 0.01, 0.02, 0.05, 0.1, 0.15, 0.2, 0.5, 1.0) of W, Mo, and Nb atoms, respectively, where the stress initially increases linearly with strain (elastic stage), followed by a sudden drop indicating the onset of plastic deformation. Fig. 4(d) shows the variation of yield stress to concentration for W, Mo, and Nb doping. For W and Mo doping, the yield stress initially decreases and then increases as c increases. At a lower concentration, the random substitution of a few W and Mo atoms with Ta atoms in the D/S region disrupts the symmetry of the $\Sigma3(11\bar{1})$ GB, leading to local stress inhomogeneity and concentration, resulting in a decrease in yield stress. As concentration increases, the strengthening influence of W and Mo atoms intensifies progressively, causing the yield stress to surpass that of the undoped Ta bicrystal sample. However, Nb doping results in a decrease in yield stress, with this decrease becoming more pronounced as concentration increases [Fig. 4(d)].

3.2.2 Deformation behavior with GB doping. The deformation behavior of samples with low concentration (c

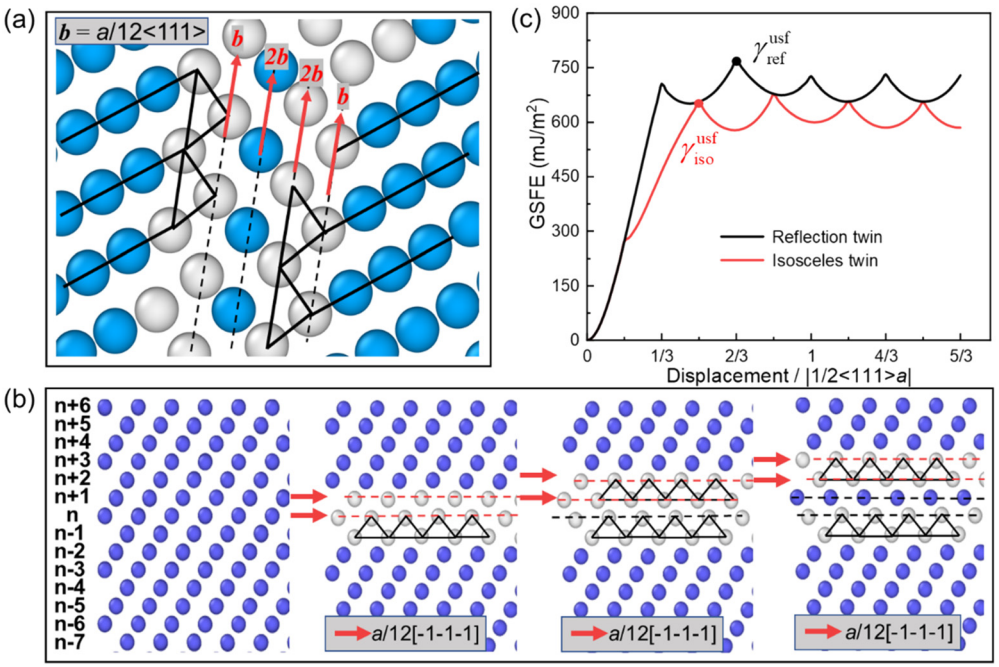

Fig. 3 Twinning mechanism in pure Ta bicrystal with $\Sigma3(11\bar{1})\langle110\rangle$ GB under shear. (a) Snapshot of {110} atomic plane of the lower grain exhibiting a 4-layer isosceles twin and the relative slip of each layer. (b) Schematic illustration of isosceles twin nucleation, involving layer-by-layer movement of $a/12\langle111\rangle$ dislocations on adjacent {112} planes. (c) Generalized stacking fault energy (GSFE) curves for isosceles and reflection twins, with γ_{iso}^{usf} and γ_{ref}^{usf} denoting energy barriers for the nucleation of isosceles twins and reflection twins, respectively.

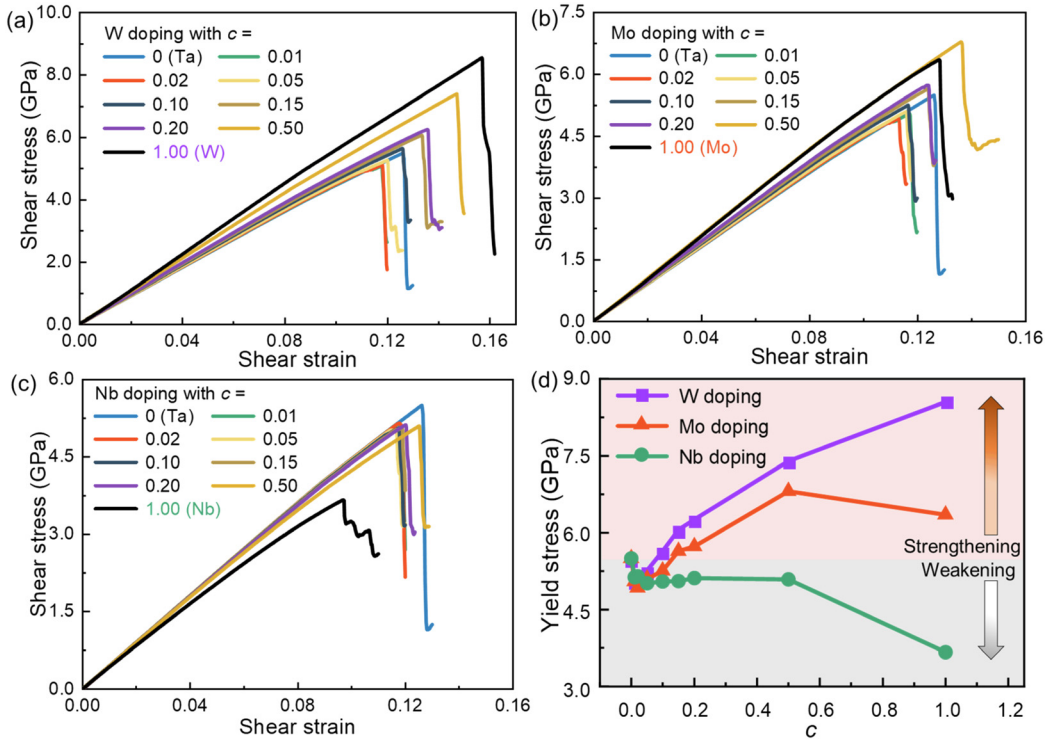

Fig. 4 Mechanical response of Ta bicrystal doped with W, Mo, and Nb atoms under shear. (a)–(c) Shear stress–strain curves of samples doped with various concentrations of W, Mo, and Nb atoms. (d) Variation of yield stress with doping concentration.

$\leq$ 0.2) doping is primarily governed by dislocation slip in the upper grain and twinning in the lower grain, similar to the observations in Fig. 2. However, as c increases, a transition in the deformation behavior occurs. Fig. 5(a) shows the atomic distribution in the D/S region of the sample for W, Mo, and Nb doping at c = 0.5. In the case of W doping, a phase transformation from BCC to FCC occurs in the non-D/S region of the lower grain near the yield point [Fig. 5(b) γ = 0.1392, with yield strain γ_y = 0.1472]. With the increase of γ, twins and $a/2\langle 111\rangle$ edge dislocations nucleate from the GB and propagate inward into the lower and upper grains, respectively. As twins form and expand, the accumulated elastic strain energy is released, inducing a partial transformation of the FCC structure back to BCC structure [highlighted in black dashed boxes in Fig. 5(b) γ = 0.1476]. For Mo doping, a similar deformation behavior is observed, albeit with a relatively smaller phase transformation region, as shown in Fig. 5(c) γ = 0.1366. However, in the case of Nb doping, the location of the phase transformation differs, as shown in Fig. 5(d). At γ = 0.1224, the phase transformation takes place in the D/S region of the lower grain near the yield point (γ_y = 0.1252), contrasting with the phase transformation location observed in W and Mo doping scenarios, which predominantly occur in the non-D/S region. Comparable deformation-induced structural transformations have also been reported in various BCC materials, such as Mo,[53] Fe,[54] Nb,[55] and high entropy alloys.[56,57]

3.3 Effect of GB segregation

Fig. 6(a)–(c) show the shear stress–strain curves of samples segregated with various concentrations (c = 0.01, 0.02, 0.05, 0.1, 0.15, 0.2) of W, Mo, and Nb atoms, respectively. Fig. 6(d) depicts the relationship between yield stress and concentration for both GB doping and GB segregation, revealing that the strengthening effect of GB segregation is more pronounced than that of GB doping. Specifically, Nb doping results in a decrease in the yield stress, while Nb segregation significantly improves them, which suggests potential alterations in the deformation behavior between the two kinds of samples.

Compared to GB doping, lower concentration GB segregation can induce phase transformations under shear, as shown in Fig. 7. For W and Mo segregation, the phase transformation occurs in the non-D/S region [Fig. 7(a) and (b)]. However, Nb segregation triggers large-scale phase transformations in both the D/S and non-D/S region [-Fig. 7(c)], which differs from the transformation location observed in Nb doping, where it occurs solely in the D/S region [Fig. 5(d)]. Both W/Mo doping/segregation and Nb segregation enhance the yield stress of Ta bicrystal samples, with phase transformations occurring in the non-D/S regions during shear. Conversely, Nb doping reduces the yield stress, with the phase transformation occurring in the D/S region. In summary, for Ta GB doping/segregation, phase transformations in the non-D/S region are associated with enhanced yield stress, whereas those in the D/S region tend

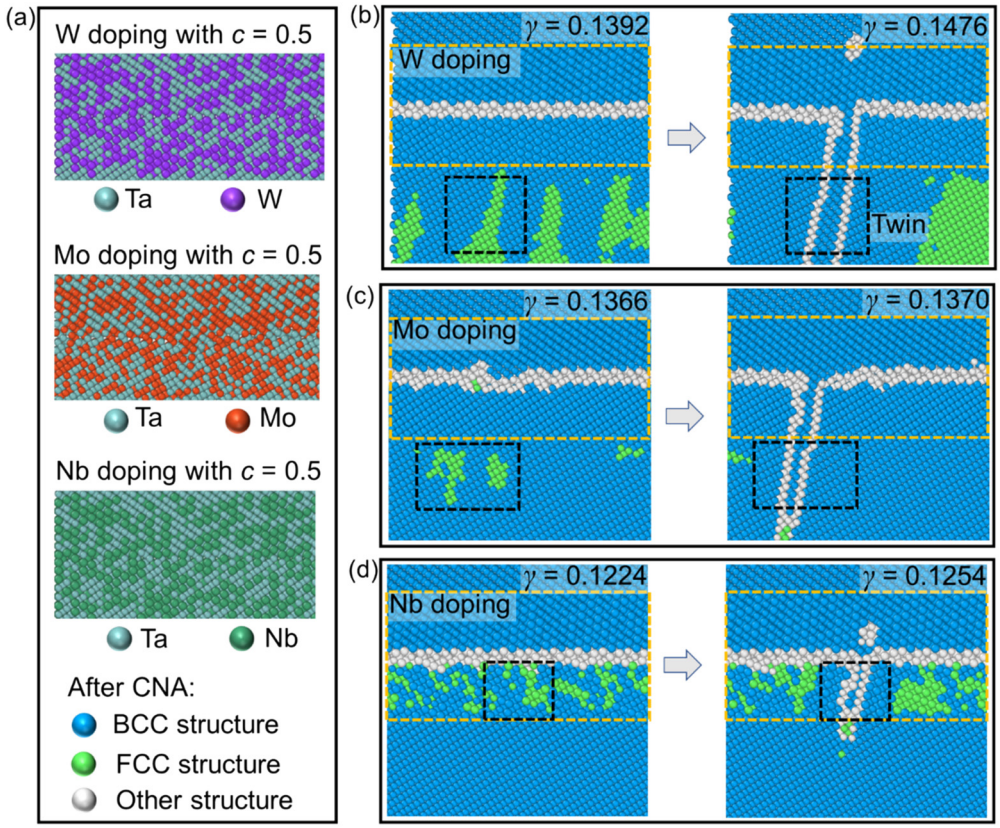

Fig. 5 Deformation behaviors of Ta bicrystals doped by high-concentration (c = 0.5) W, Mo, and Nb atoms under shear. (a) Atomic distribution in the D/S region for W, Mo, and Nb doping, colored with atomic type. (b) and (c) Microstructure evolution of sample with W and Mo doping: phase transformation in the non-D/S region of the lower grain, followed by twin nucleation and reverse phase transformation; (d) microstructure evolution of sample with Nb doping: phase transformation and reverse phase transformation in the D/S region of the lower grain, colored with CNA: blue and green atoms represent BCC and FCC structures, respectively, while white atoms represent other structures.

to result in yield stress deterioration. Further discussion on this topic will be provided later.

4. Discussion

4.1 Competition between dislocation glide and twinning

In both pure Ta bicrystal samples and samples with GB doping or segregation, plastic deformation under shear involves dislocation slip in the upper grain and twinning in the lower grain. This raises the question of why twinning occurs in the lower grain while dislocation slip predominates in the upper grain. Our analysis, illustrated in Fig. 2 and 3, shows that edge dislocations form in the upper grain as atomic layers on the (112) planes slide along the $[11\bar{1}]$ direction by a distance of $|1/2\langle 111\rangle a|$ (a is the lattice constant). While the isosceles twins in the lower grain originate from the slipping of $a/12\langle 111\rangle$ partial dislocations layer by layer along the $[\bar{1}\bar{1}\bar{1}]$ direction on adjacent $(11\bar{2})$ planes. Although both mechanisms involve atomic movements on the $\{112\}\langle 111\rangle$ slip system, they result in distinct plastic behaviors. In BCC metals, the atomic arrangement on the $\{112\}$ plane exhibits twinning–antitwinning asymmetry along the $\langle 111\rangle$ direction.[58–60] Specifically, for the $(11\bar{2})$ plane, the $[\bar{1}\bar{1}\bar{1}]$ direction serves as the twinning direction, favoring twinning in the lower grain; whereas for the (112) plane, the $[11\bar{1}]$ direction acts as the antitwinning direction, promoting dislocation slip in the upper grain.

To deepen the understanding of this asymmetry, we calculate the GSFE curves for the nucleation of dislocations and twins along both twinning and anti-twinning directions. The GSFE for twin nucleation along the anti-twinning direction is calculated based on the two-layer by two-layer staggered shuffle nucleation mechanism proposed by Wei *et al.*[60,61] The results are presented in Fig. 8, where γ^{usf} is the unstable stacking fault energy for dislocation nucleation, γ_T^{usf} and γ_{AT}^{usf} are the unstable stacking fault energies for twin nucleation along the twinning and antitwinning directions, respectively. During shear along the positive X-axis, the atomic layers of the $\{112\}$ plane in the lower grain glide along the twinning direction. The energy barrier required for twin nucleation (γ_T^{usf}) in this direction is significantly lower than that for dislocation nucleation (γ^{usf}), as shown in Fig. 8(a), making twinning more favorable in the lower grain. Conversely, the upper grain exhibits the opposite behavior [-Fig. 8(b)], leading to dislocation slip. Therefore, if the shear direction is altered to the negative X-axis, twinning would occur in the upper grain while dislocation slip would take

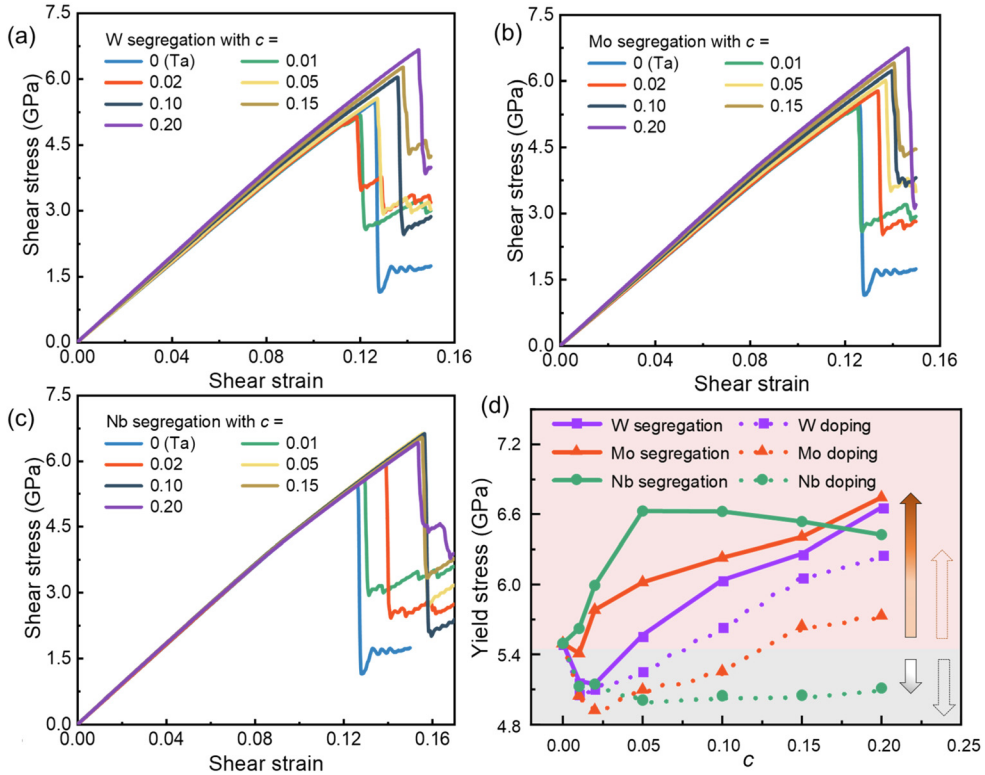

Fig. 6 Mechanical response of Ta bicrystal sample with W, Mo, and Nb segregation under shear. (a)–(c) Shear stress–strain curves of samples with different segregation concentrations of W, Mo, and Nb. (d) Relationship between the yield stress and type/concentration of doping/segregation elements. GB segregation exhibits a more pronounced strengthening effect on mechanical properties compared to GB doping.

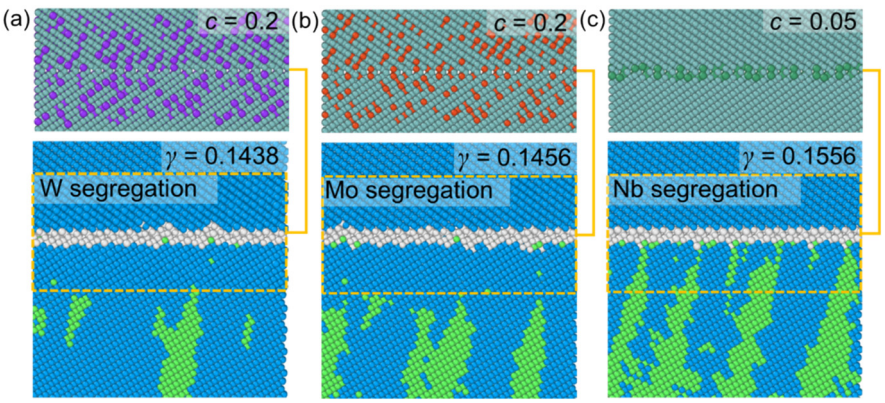

Fig. 7 Locations of phase transformation in Ta bicrystal samples with W, Mo, and Nb segregation under shear. (a) and (b) For W and Mo segregation, phase transformations occur in the same region as in samples with W and Mo doping. (c) Nb segregation induces phase transformations in the non-D/S region, differing from the location observed in the sample with Nb doping.

place in the lower grain. The shear results along different directions, presented in Fig. 8(c), validate this hypothesis.

4.2 Phase transformation mechanism

During shear, a phase transformation from BCC to FCC is observed in samples with GB doping and segregation. This transformation is commonly explained by the Bain relation.[62] Fig. 9(a) shows four adjacent BCC unit cells, with blue balls representing corner atoms and green balls depicting body-centered atoms. The structure connected by green lines is known as face-centered tetragonal (FCT) lattice, which resembles the FCC structure with atoms at the centers of each face. When the lengths and widths of the faces in the FCT structure become equal, it exhibits the characteristics of FCC structure, leading to the transformation from BCC to FCC.

For the BCC to FCC phase transformation to take place, three essential conditions should generally be met:[53] high shear stress, large elastic strain energy, and suppression of

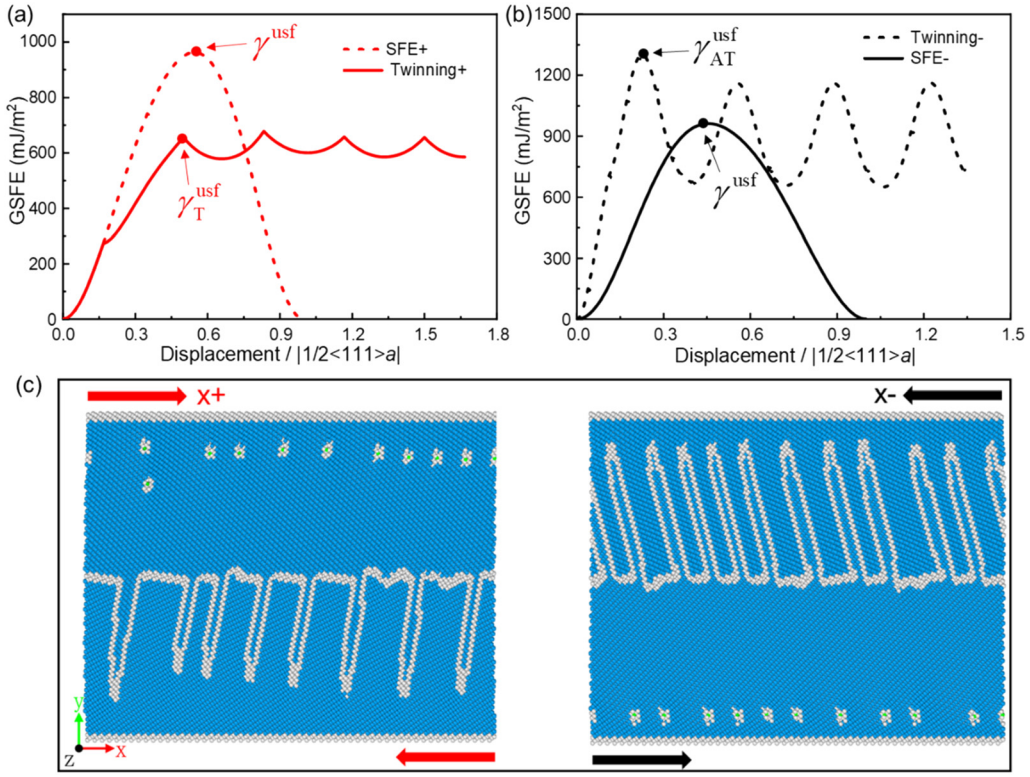

Fig. 8 Competition between dislocation slip and twinning. (a) and (b) GSFE curves for dislocation and twin nucleation along the twinning and antitwinning direction, respectively. γ^{usf} denotes the unstable stacking fault energy for dislocation nucleation, γ_T^{usf} and γ_{AT}^{usf} are the unstable stacking fault energies for twin nucleation along the twinning and antitwinning direction, respectively. (c) Influence of shear direction on dislocation slip and twinning locations.

twinning deformation. During loading, the suppression of twinning deformation inhibits the loose of shear stress and the release of elastic strain energy. The combination of high shear stress and large elastic strain energy drives the low-energy BCC structure to transform into the high-energy FCC structure.[53]

For instance, in the case of W doping with c = 0.5, as shown in the left figure of Fig. 9(b), phase transformation (in green) occurs in the non-D/S region of the lower grain. At γ = 0.1368 and τ = 6.92 GPa (close to the yield point: γ_y = 0.1472, τ_y = 7.39 GPa), the presence of W atoms impedes atomic movement in the D/S region, thereby suppressing twinning deformation at the GB. As the elastic strain energy accumulates, the $(11\bar{2})$ atomic layers in the non-D/S region glide along the $[\bar{1}\bar{1}1]$ direction [left figure in Fig. 9(b)], resulting in a larger strain compared to the D/S region [strain contour plot in the middle figure of Fig. 9(b)]. However, the relative immobility of atoms in the D/S region leads to uncoordinated atomic motion in the non-D/S region, prompting the BCC to FCC phase transformation, as illustrated in the schematic diagram on the right figure of Fig. 9(b). Consequently, the phase transformation occurs in the non-D/S region (pure Ta), indicating the reinforcement of the D/S region and thereby enhancing the mechanical properties of samples with GB segregation or W, Mo doping. Conversely, the phase transformation in the D/S region results in a reduction in the mechanical properties of the sample with Nb doping. Despite the absence of phase transformation in the non-D/S region of the samples with low concentration GB segregation and W, Mo GB doping [-Fig. 9(c)], there is still a positive effect on increasing the yield stress of the samples. This is attributed to the limited strengthening ability of low-concentration GB segregation/doping on the D/S region. The non-uniform movement distance of the {112} planes in the non-D/S region is insufficient to facilitate the complete conversion from BCC to FCC before the activation of twinning deformation. The activation of twinning results in the release of elastic strain energy, thereby preventing the occurrence of phase transformation. Nevertheless, there remains a noticeable preferential motion of atoms in the non-D/S region, as shown in Fig. 9(c).

During the shear process, whether through GB doping or GB segregation, phase transformation does not occur in the upper grain due to the twinning–antitwinning asymmetry inherent in the BCC structure. As previously analyzed, phase transformation arises from the non-uniform motion of {112} plane atoms along the ⟨111⟩ direction. When sheared along the positive X-axis direction, atoms on the {112} plane of the lower grain move along the twinning direction, while those of the upper grain move along the antitwinning direction.

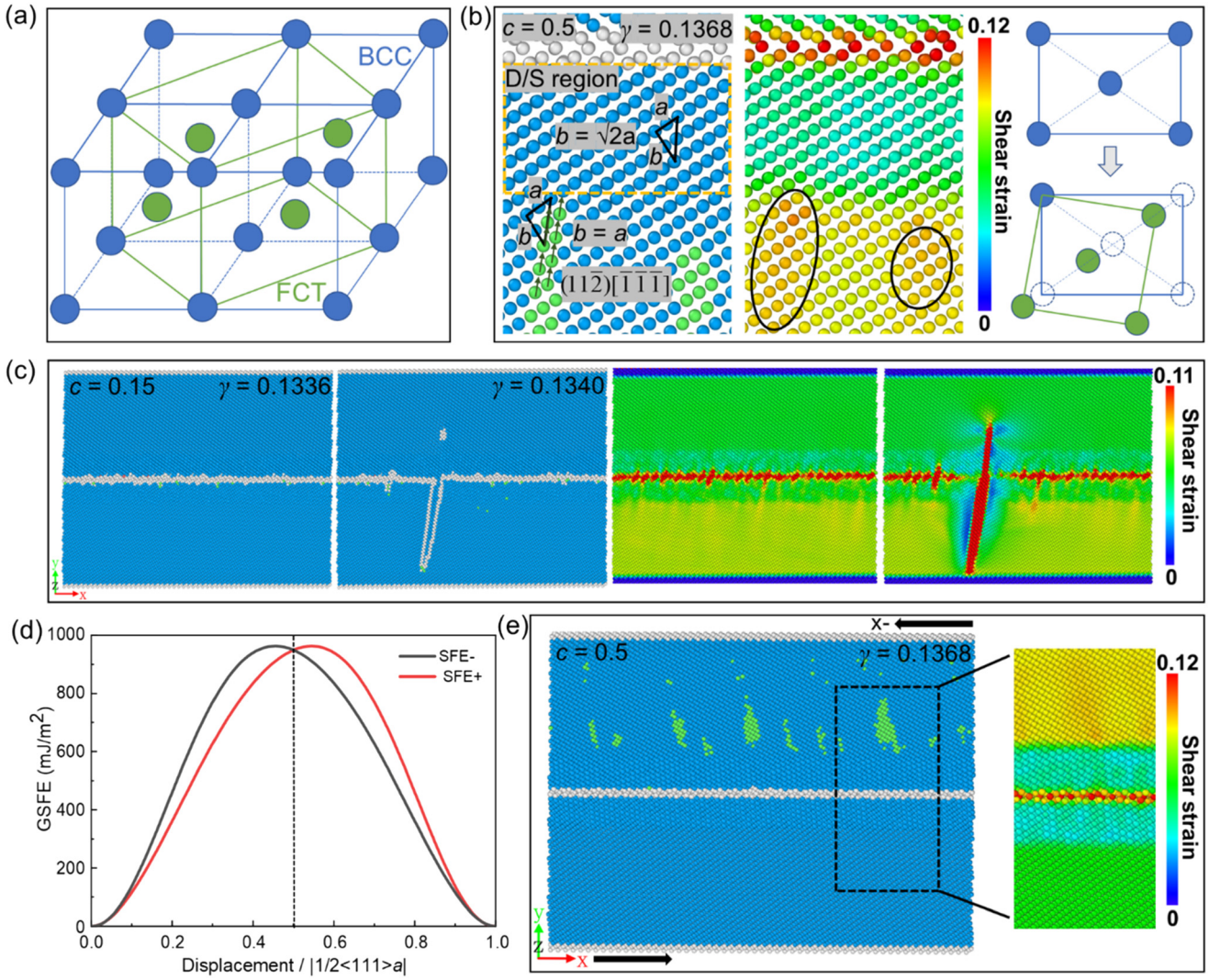

Fig. 9 Phase transformation mechanisms under shear. (a) Crystallographic relationship between BCC and FCC. (b) BCC to FCC transformation in samples with W doping (c = 0.5): driven by the non-uniform motion of {112} planes in non-D/S region of lower grain along ⟨111⟩ direction. (c) W doping with c = 0.15: no phase transformation in the non-D/S region, strengthening of D/S region indicated by greater strain in the non-D/S region than that in the D/S region. (d) SFE curves of {112} planes in BCC Ta along twinning and antitwinning directions. (e) Reverse shear of the sample with W doping at c = 0.5: phase transformation occurs in the non-D/S region of the upper grain.

The GSFE curves of the {112} planes along these directions, depicted in Fig. 9(d) with "+" and "–" symbols representing the twinning and antitwinning directions, respectively, exhibit an antisymmetric relationship with respect to X = 0.5.

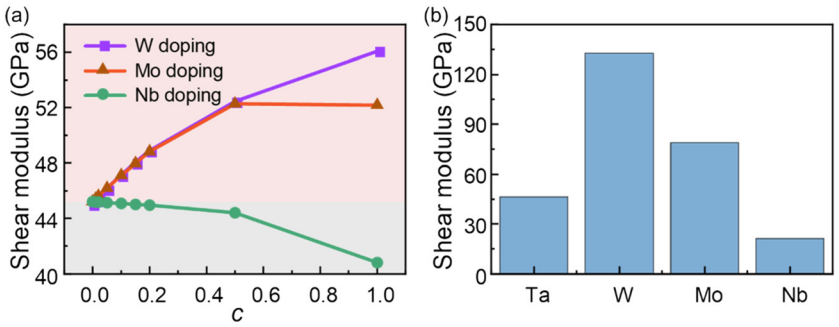

Fig. 10 Effect of GB doping on the shear modulus. (a) Variation of shear modulus with type/concentration of foreign elements. (b) Comparison of the shear modulus of pure Ta, W, Mo, and Nb.

The maximum SFE of the antitwinning direction precedes that of the twinning direction, with all SFE− values exceeding SFE+ when $X < 0.5$. This suggests that the {112} plane atomic layers exhibit easier movement along the twinning direction, facilitating phase transformation in the lower grain. Upon reversing the shear direction (negative X-axis), the {112} plane atomic layers in the upper grain move along the twinning direction, while those in the lower grain move along the opposite direction. Consequently, a larger shear strain in the non-D/S region of the upper grain compared to the lower grain, leads to phase transformation in the upper grain, as shown in Fig. 9(e).

4.3 Effects of GB doping and segregation on mechanical properties

As shown in Fig. 4(d) and 10(a), the shear mechanical properties of samples with GB doping are influenced by the type and concentration of foreign elements. When concentration is low, the addition of a small number of doping atoms disrupts the symmetry of the $\Sigma3(11\bar{1})$ GB, leading to a decrease in the yield stress. As concentration increases, W and Mo doping enhance mechanical properties, while Nb doping has the opposite effect. The shear modulus of samples with various doping elements exhibits a similar trend to the yield stress as concentration varies. Fig. 10(b) shows the shear modulus of pure W, Mo, and Nb bicrystal samples, where the ranking (W > Mo > Ta > Nb) corresponds to the influence degree of each doping element on the mechanical properties of Ta bicrystals.

Compared to GB doping, GB segregation has a more pronounced strengthening effect on yield stress [Fig. 6(d)]. The segregation of foreign atoms into GBs modifies their structure and energy, crucial factors that determine their stability and influence mechanical response by altering dislocation nucleation and motion pathways.[24,25,63,64] Taking Nb segregation as an example, which exhibits the most significant strengthening effect, Fig. 11(a) reveals extensive "GB coarsening" in the sample with 2% Nb doping both before and after twinning and dislocation nucleation, resulting in a metastable B-type GB structure. This phenomenon arises from the partial slip of the atoms at the second site in the initial GB structure [inset in Fig. 11(a)] along the $(112)[11\bar{1}]$ slip system. Conversely, in Fig. 11(b), when Nb atoms (red atoms) segregate to the second site of GB, there is no significant "GB coarsening" before and after the nucleation of twins and dislocations. The segregation of Nb atoms at the GB maintains the original A-type GB structure, thereby enhancing GB stability.

GBs typically have higher energy than the grain interior and often serve as preferred nucleation sites for dislocations. The GB energy after doping or segregation is calculated with $E^{X}_{GB} = (E^{X}_{bicrystal} - E^{X}_{bulk})/2A$, where $E^{X}_{bicrystal}$ and E^{X}_{bulk} are the total energies of Ta bicrystal and Ta bulk with the addition of

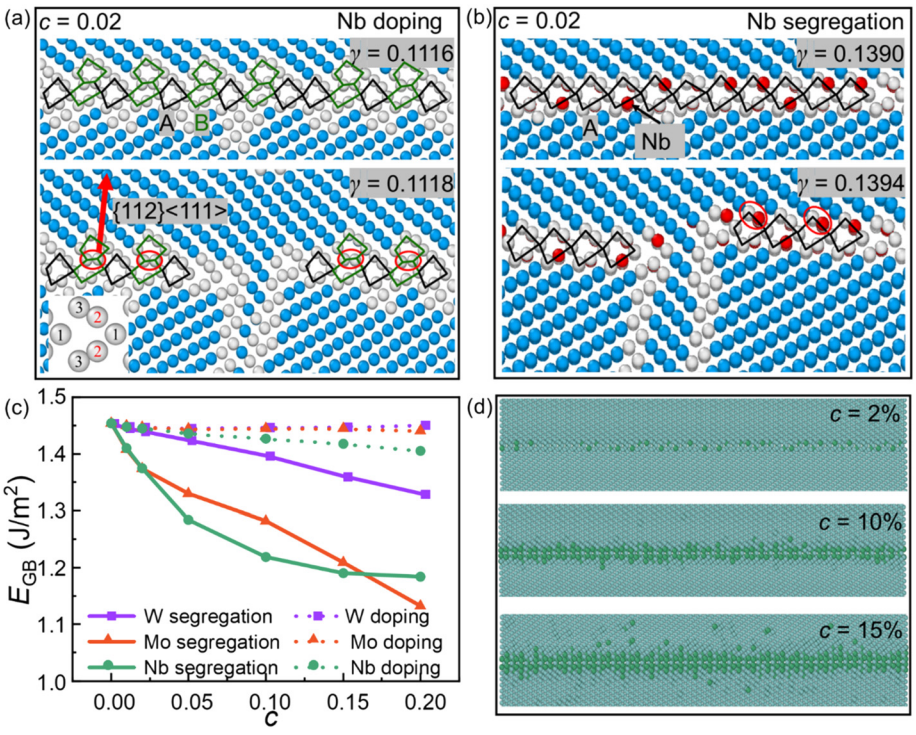

Fig. 11 The effect of GB segregation and doping on GB structure and energy. (a) GB coarsening occurs in Nb doping samples. (b) The segregation of Nb atoms to the second site of the GB structure reduces the occurrence of metastable GB structures (type B) and enhances GB stability. (c) Relationship between GB energy and type/concentration of doping/segregation elements. GB doping minimally affects GB energy, while GB segregation significantly reduces it. (d) Atomic distribution within the D/S region of samples with Nb segregation at varying concentrations.

X (X = W, Mo, and Nb) atoms, respectively, and A represents the GB area. The results are shown in Fig. 11(c). For GB doping, the type and concentration of foreign atoms have a slight effect on GB energy. Even with notable changes in Nb doping, the variation in GB energy is only 0.04 J m^{-2}, which accounts for 2.7% of the GB energy of pure Ta bicrystal. In contrast, GB segregation markedly reduces GB energy, with this reduction persisting as concentration increases. The lower GB energy post-segregation signifies a more stable GB structure, which is more beneficial for strengthening the D/S region. Consequently, with identical concentrations of foreign atoms, GB segregation is more prone to inducing phase transformation within the non-D/S region of the sample (Fig. 7), in contrast to GB doping. W and Mo segregation, characterized by their high shear modulus and low GB energy, synergistically enhance mechanical properties, resulting in increased yield stress with rising concentration. However, for Nb segregation, a critical point is observed at c = 0.05: the yield stress rises with increasing concentration when $c < 0.05$, but decreases when $c > 0.05$ [Fig. 6(d)]. When concentration is low, Nb atoms fully segregate to the GB [Fig. 11(d)]; however, as concentration increases, not all Nb atoms can be accommodated by the GB, resulting in a combination of GB segregation and low-concentration GB doping. Unfortunately, low-concentration Nb doping diminishes mechanical properties, with this decline worsening as doping concentration increases [Fig. 4(d)]. Consequently, when $c >$ 0.05, the yield stress progressively decreases with increasing concentration.

In summary, GB segregation significantly reduces GB energy compared to GB doping. The segregation of foreign atoms to the second site of the GB effectively inhibits the formation of metastable GB structures. This is crucial, as the slip of atoms at this second site in the initial GB structure is key to activating the $\{112\}\langle 111\rangle$ slip system. Consequently, this segregation enhances GB stability, making it more effective in strengthening the material than GB doping.

In addition to high-energy symmetric tilt $\Sigma 3(11\bar{1})\langle 110\rangle$ GB, low-energy $\Sigma 3\{112\}\langle 110\rangle$ GBs are also observed in BCC metals.[45] To check whether these findings also hold in other types of GBs, we create Ta bicrystal samples with $\Sigma 3\{112\}\langle 110\rangle$ GBs and conduct MD simulations to investigate their shear mechanical properties under various doping and segregation conditions. For GB doping, as shown in Fig. S1(a)–(c) in ESI,† the shear stress–strain curves exhibit a serrated fluctuation pattern. Notably, W and Mo doping enhances the shear yield stress of $\Sigma 3\{112\}$ Ta bicrystals, whereas Nb doping has an opposing effect, as shown in Fig. S1(d).† For GB segregation, the shear stress–strain curves retain the serrated shape [Fig. S2(a)–(c)†], and Fig. S2(d)† shows that the segregation of W, Mo, and Nb enhances mechanical properties, with segregation showing a more pronounced strengthening effect compared to those from GB doping. These observations are consistent with those from the sample with $\Sigma 3(11\bar{1})\langle 110\rangle$ high-energy symmetric tilt GB.

However, it is important to note that GBs exhibit five degrees of freedom, including variations in symmetry, asymmetry, tilting, and twisting, leading to diverse thermal and mechanical behaviors. The GBs examined in our work represent only a narrow segment of the five-degree freedom GB space. To achieve a comprehensive understanding of GB behavior and the effects of element segregation on mechanical properties, further research across a wider variety of GBs is necessary.

5. Conclusions

In this work, the shear deformation behaviors and mechanical properties of Ta bicrystals with $\Sigma 3(11\bar{1})\langle 110\rangle$ high-energy symmetric tilt GB under various element doping/segregation conditions are investigated using MD simulation. The main conclusion can be drawn as follows.

1) In pure Ta bicrystals, the shear deformation behavior involves dislocation glide and twinning. Four-layer isosceles twins are energetically more favorable compared to reflection twins. The competition between dislocation glide and twinning is attributed to twinning–antitwinning asymmetry in the BCC structure.

2) Introducing foreign atoms into Ta bicrystals affects their mechanical behavior. Specifically, W and Mo doping, characterized by a higher shear modulus than Ta, enhances the yield stress, while Nb doping, with a lower shear modulus, exhibits the opposite effect. Moreover, increasing doping concentration induces a BCC to FCC phase transformation. This transformation occurs due to the non-uniform motion of $\{112\}$ plane atoms along the $\langle 111\rangle$ direction, and the diverse types of doping elements result in varying phase transformation locations.

3) GB segregation of W, Mo, and Nb atoms enhances the mechanical properties more effectively than GB doping. It significantly reduces GB energy, especially with higher segregation concentration. Solute atom segregation alters GB composition, enhances structural stability, and suppresses "GB coarsening" during shear, contrasting with the minimal effect of GB doping on GB energy.

In this work, we elucidated the competitive relationship between dislocation glide and twinning in BCC Ta during shear based on the fact of the twinning–antitwinning asymmetry, which is intrinsic to the atomic arrangement characteristics of the BCC structure. Therefore, these results may also apply to other BCC metals. Additionally, we examined the effects of GB segregation and doping on the yield stress of Ta bicrystal by analyzing GB structure and energy. This analysis offers valuable insights into the composition, structure, and properties of Ta GBs, which could guide future research on GB modification in other BCC metals and aid in the design of Ta-based alloys with desired performances based on GB segregation engineering.

Data availability

The data that support the findings of this study are available from the corresponding author upon reasonable request.

Author contributions

Yang Pan: conceptualization, formal analysis, methodology, writing – original draft, writing – review & editing. Tao Fu: conceptualization, formal analysis, funding acquisition, investigation, methodology, software, validation, writing – original draft, writing – review & editing. Hao Hu: methodology, validation. Xingjie Chen: formal analysis, validation. Chuanying Li: investigation, methodology. Shayuan Weng: formal analysis, methodology, writing – review & editing.

Conflicts of interest

There are no conflicts to declare.

Acknowledgements

This work was supported by the National Natural Science Foundation of China (11932004, and 12272066), the Fundamental Research Funds for the Central Universities (2024CDJXY009), and the Natural Science Foundation of Chongqing Municipality (CSTB2022NSCQ-MSX0383).

References

1 R. B. Figueiredo, M. Kawasaki and T. G. Langdon, *Prog. Mater. Sci.*, 2023, **137**, 101131.
2 M. A. Meyers, A. Mishra and D. J. Benson, *Prog. Mater. Sci.*, 2006, **51**, 427–556.
3 T. Wang, M. Zha, C. Du, H.-L. Jia, C. Wang, K. Guan, Y. Gao and H.-Y. Wang, *Mater. Res. Lett.*, 2023, **11**, 187–195.
4 Z. Wang, H. Wu, Y. Wu, H. Huang, X. Zhu, Y. Zhang, H. Zhu, X. Yuan, Q. Chen, S. Wang, X. Liu, H. Wang, S. Jiang, M. J. Kim and Z. Lu, *Mater. Today*, 2022, **54**, 83–89.
5 J. Cui, L. Ma, G. Chen, N. Jiang, P. Ke, Y. Yang, S. Wang, K. Nishimura and J. Llorca, *Mater. Sci. Eng., A*, 2023, **862**, 143826.
6 Y. J. Jin, H. Lu, C. Yu and J. J. Xu, *Mater. Charact.*, 2013, **84**, 216–224.
7 V. Randle, *Mater. Sci. Technol.*, 2010, **26**, 253–261.
8 X. Zhou and J. Song, *Acta Mater.*, 2018, **148**, 9–17.
9 S. N. Naik and S. M. Walley, *J. Mater. Sci.*, 2020, **55**, 2661–2681.
10 K. Lu, *Nat. Rev. Mater.*, 2016, **1**, 16019.
11 C. C. Koch, *J. Mater. Sci.*, 2007, **42**, 1403–1414.
12 C. C. Koch, R. O. Scattergood, K. A. Darling and J. E. Semones, *J. Mater. Sci.*, 2008, **43**, 7264–7272.
13 D. Raabe, M. Herbig, S. Sandlöbes, Y. Li, D. Tytko, M. Kuzmina, D. Ponge and P. P. Choi, *Curr. Opin. Solid State Mater. Sci.*, 2014, **18**, 253–261.
14 S. Jang, Y. Purohit, D. L. Irving, C. Padgett, D. Brenner and R. O. Scattergood, *Acta Mater.*, 2008, **56**, 4750–4761.
15 Q. Li, J. Zhang, H. Tang, H. Ye and Y. Zheng, *Nanotechnology*, 2019, **30**, 275702.
16 L. Fan, T. Yang, J. H. Luan and Z. B. Jiao, *J. Alloys Compd.*, 2020, **832**, 154903.
17 Z. Xiao, J. Hu, Y. Liu, F. Dong and Y. Huang, *Mater. Sci. Eng., A*, 2019, **756**, 389–395.
18 D. Zhao, O. M. Løvvik, K. Marthinsen and Y. Li, *Acta Mater.*, 2018, **145**, 235–246.
19 F. Meng, X. Lu, Y. Liu and Y. Qi, *J. Mater. Sci.*, 2017, **52**, 4309–4322.
20 X. Wang and L. Benabou, *J. Eng. Mater. Technol.*, 2018, **140**, 011008.
21 K.-i. Ebihara and T. Suzudo, *Modell. Simul. Mater. Sci. Eng.*, 2018, **26**, 065005.
22 N. Miyazawa, M. Hakamada and M. Mabuchi, *Philos. Mag. Lett.*, 2017, **97**, 311–319.
23 J. Wang, R. Janisch, G. K. H. Madsen and R. Drautz, *Acta Mater.*, 2016, **115**, 259–268.
24 N. Ma, D. Zhao, C. Shi, C. He, E. Liu, J. Sha, Y. Li and N. Zhao, *J. Mater. Sci.*, 2022, **57**, 21591–21606.
25 S. Pal, K. Vijay Reddy and D. E. Spearot, *J. Mater. Sci.*, 2020, **55**, 6172–6186.
26 L. Y. Yang, C. Y. Wu, D. K. Peng, Y. J. Shen, J. L. Fan and H. R. Gong, *Vacuum*, 2023, **208**, 111712.
27 G. Zhang, G. Chen, C. Panwisawas, X. Teng, Y. Ma, R. An, Y. Huang, J. Cao and X. Leng, *Acta Mater.*, 2023, **261**, 119387.
28 H. Xue, Y. Wu, F. Tang, X. Li, X. Lu, J. Ren and J. Li, *Mater. Today Commun.*, 2022, **31**, 103319.
29 C. J. Marvel, K. D. Behler, J. C. LaSalvia, R. A. Haber and M. P. Harmer, *Acta Mater.*, 2022, **227**, 117684.
30 W. Y. Liang, L. Sun, Y. C. Jiang, L. Y. Yang, H. R. Gong, J. L. Fan and T. Liu, *J. Phys. Chem. Solids*, 2022, **165**, 110687.
31 F.-Z. Dai, Y. Sun, Y. Ren, H. Xiang and Y. Zhou, *J. Mater. Sci. Technol.*, 2022, **101**, 234–241.
32 X. Wu, Y.-W. You, X.-S. Kong, J.-L. Chen, G. N. Luo, G.-H. Lu, C. S. Liu and Z. Wang, *Acta Mater.*, 2016, **120**, 315–326.
33 Y. Pan, T. Fu, M. Duan, C. Li, H. Hu and X. Peng, *ACS Appl. Nano Mater.*, 2024, **7**, 8121–8129.
34 H. Hu, T. Fu, C. Li and X. Peng, *J. Mater. Res. Technol.*, 2023, **27**, 7159–7166.
35 S. Xu, A. Al Mamun, S. Mu and Y. Su, *J. Alloys Compd.*, 2023, **959**, 170556.
36 Z. Bai, T. Fu, H. Hu, W. Yu and X. Peng, *Comput. Mater. Sci.*, 2024, **235**, 112837.
37 N. Kvashin, N. Anento and A. Serra, *Phys. Rev. Mater.*, 2022, **6**, 053607.
38 N. Kvashin, N. Anento, D. Terentyev and A. Serra, *Phys. Rev. Mater.*, 2022, **6**, 033606.
39 J. Li, X. Yang and P. Wang, *J. Mater. Res.*, 2021, **36**, 775–783.
40 E. N. Hahn, S. J. Fensin, T. C. Germann and M. A. Meyers, *Scr. Mater.*, 2016, **116**, 108–111.
41 M. A. Tschopp and D. L. McDowell, *Philos. Mag.*, 2007, **87**, 3147–3173.

42 D. Aksoy, M. J. McCarthy, I. Geiger, D. Apelian, H. Hahn, E. J. Lavernia, J. Luo, H. Xin and T. J. Rupert, *J. Appl. Phys.*, 2022, **132**, 235302.
43 B. Sadigh, P. Erhart, A. Stukowski, A. Caro, E. Martinez and L. Zepeda-Ruiz, *Phys. Rev. B: Condens. Matter Mater. Phys.*, 2012, **85**, 184203.
44 X.-G. Li, C. Chen, H. Zheng, Y. Zuo and S. P. Ong, *npj Comput. Mater.*, 2020, **6**, 70.
45 X. Chen, Y. Pan, S. Weng, H. Hu, C. Li and T. Fu, *J. Mater. Res. Technol.*, 2024, **30**, 8999–9006.
46 S. Plimpton, *J. Comput. Phys.*, 1995, **117**, 1–19.
47 A. Stukowski, *Modell. Simul. Mater. Sci. Eng.*, 2010, **18**, 015012.
48 A. Stukowski, V. V. Bulatov and A. Arsenlis, *Modell. Simul. Mater. Sci. Eng.*, 2012, **20**, 085007.
49 D. Faken and H. Jónsson, *Comput. Mater. Sci.*, 1994, **2**, 279–286.
50 H. Tsuzuki, P. S. Branicio and J. P. Rino, *Comput. Phys. Commun.*, 2007, **177**, 518–523.
51 Q. S. Huang, Q. K. Zhao, H. F. Zhou and W. Yang, *Int. J. Plast.*, 2022, **159**, 103466.
52 A. W. Sleeswyk, *Philos. Mag.*, 1963, **8**, 1467–1486.
53 S. J. Wang, H. Wang, K. Du, W. Zhang, M. L. Sui and S. X. Mao, *Nat. Commun.*, 2014, **5**, 3433.
54 K. P. Zolnikov, A. V. Korchuganov and D. S. Kryzhevich, *Comput. Mater. Sci.*, 2018, **155**, 312–319.
55 Q. Wang, J. Wang, J. Li, Z. Zhang and S. X. Mao, *Sci. Adv.*, 2018, **4**, eaas8850.
56 B. Ding, H. Y. Song, M. R. An, M. X. Xiao and Y. L. Li, *J. Appl. Phys.*, 2021, **130**, 244301.
57 W. Jian and L. Ren, *Int. J. Plast.*, 2024, **173**, 103867.
58 M. S. Duesbery and V. Vitek, *Acta Mater.*, 1998, **46**, 1481–1492.
59 J. W. Wang, Z. Zeng, M. R. Wen, Q. N. Wang, D. K. Chen, Y. Zhang, P. Wang, H. T. Wang, Z. Zhang, S. X. Mao and T. Zhu, *Sci. Adv.*, 2020, **6**, eaay2792.
60 G. B. Wei, H. X. Xie, F. X. Yin and G. H. Lu, *Phys. Rev. Mater.*, 2021, **5**, 123604.
61 G. B. Wei, H. X. Xie and G. H. Lu, *Philos. Mag.*, 2023, **103**, 1442–1452.
62 G. L. Krasko and G. B. Olson, *Phys. Rev. B: Condens. Matter Mater. Phys.*, 1989, **40**, 11536–11545.
63 T. Frolov, D. L. Olmsted, M. Asta and Y. Mishin, *Nat. Commun.*, 2013, **4**, 1899.
64 Y.-J. Hu, Y. Wang, W. Y. Wang, K. A. Darling, L. J. Kecskes and Z.-K. Liu, *Comput. Mater. Sci.*, 2020, **171**, 109271.

